JOURNAL OF SYNCHROTRON RADIATION
ISSN 1600-5775

First pump–probe–probe hard X-ray diffraction experiments with a 2D hybrid pixel detector developed at the SOLEIL synchrotron

Diana Bachiller-Perea,[a]* Yves-Marie Abiven,[a] Jérôme Bisou,[a] Pierre Fertey,[a] Pawel Grybos,[b] Amélie Jarnac,[a] Brahim Kanouté,[a] Anna Koziol,[b] Florent Langlois,[a] Claire Laulhé,[a,c] Fabien Legrand,[a] Piotr Maj,[b] Claude Menneglier,[a] Arafat Noureddine,[a] Fabienne Orsini,[a] Gauthier Thibaux[a] and Arkadiusz Dawiec[a]

[a]SOLEIL Synchrotron, L'Orme des Merisiers, Saint-Aubin – BP 48, 91190 Gif-sur-Yvette Cedex, France, [b]Department of Measurement and Electronics, AGH University of Science and Technology, av. A. Mickiewicza 30, Krakow 30-059, Poland, and [c]Université Paris-Saclay (Université Paris-Sud), F-91405 Orsay Cedex, France. *Correspondence e-mail: dianabachillerperea@gmail.com

Received 31 July 2019
Accepted 17 January 2020

Edited by A. Bergamaschi, Paul Scherrer Institut, Switzerland

Keywords: hybrid pixel detectors; photon counting; X-ray diffraction; time-resolved experiments; pump-probe-probe.

A new photon-counting camera based on hybrid pixel technology has been developed at the SOLEIL synchrotron, making it possible to implement pump–probe–probe hard X-ray diffraction experiments for the first time. This application relies on two specific advantages of the UFXC32k readout chip, namely its high frame rate (50 kHz) and its high linear count rate (2.6 × 10^6 photons s^{-1} $pixel^{-1}$). The project involved the conception and realization of the chips and detector carrier board, the data acquisition system, the server with its specific software, as well as the mechanical and cooling systems. This article reports on in-laboratory validation tests of the new detector, as well as on tests performed at the CRISTAL beamline within the targeted experimental conditions. A benchmark experiment was successfully performed, showing the advantages of the pump–probe–probe scheme in correcting for drifts of the experimental conditions.

1. Introduction

Studies of ultrafast phenomena have become a major scientific theme, supported by ambitious experimental developments in both laser- and accelerator-related technologies. Observations of ultrafast dynamics concern all scientific disciplines: (i) chemistry, for studying reaction mechanisms or temporal evolution of solvation structures; (ii) biology, for studying functional cycles in proteins; and (iii) physics, for studying photo-induced phase transitions, coherent phenomena, as well as successions of out-of-equilibrium states triggered by a laser pulse. Fast and ultrafast processes are studied directly in the time domain, during the so-called 'pump–probe' experiments: the sample is first excited (pumped) by a laser pulse or by another stimulus (for instance, a magnetic field pulse), and then probed after a chosen delay Δt by a light pulse which can be generated by a synchrotron source.

The SOLEIL synchrotron is engaged in the development of pump–probe experiments which combine the use of short laser pulses (as pumps) and pulsed synchrotron radiation (as probes). In this particular case, the time resolution is dictated by the duration of the synchrotron light pulses. At SOLEIL, it reaches a FWHM (full width at half-maximum) of about 100 ps in standard operation, and a FWHM of 12 ps in the so-called low-α operation (Tordeux *et al.*, 2012). Pump–probe

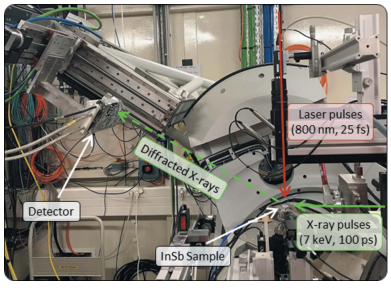

experiments are now routinely performed at the TEMPO and CRISTAL beamlines, making use of various experimental probes such as photoemission, or soft and hard X-ray scattering (Silly *et al.*, 2017; Laulhé *et al.*, 2012, 2013).

For each value of the pump–probe delay (Δt), the pump–probe cycle has to be repeated in order to generate enough statistics. The time interval between two successive laser excitations has to be longer than the full relaxation time of the sample, which typically ranges from 1 ms in dense solids to 100 ms in molecular or protein crystals. The repetition rates of pump–probe diffraction experiments thus range from 10 Hz to 1 kHz, and the available frequencies of the synchrotron light pulses are in the 1–100 MHz range. As a result, pump–probe experiments usually make use of less than a thousandth of the available photon flux. One way to increase the efficiency of this type of experiment involves adopting a pump–multiprobe scheme, in which the sample is excited and then probed multiple times before the next pump pulse is sent. MHz multiprobe schemes are especially well adapted to the study of fast dynamics, *i.e.*, on the µs timescale, which is relevant for studies of long-lived excited states in complex molecules (see, for example, Moonshiram *et al.*, 2018). When measuring ultrafast dynamics (*i.e.*, on sub-ns timescales), the pump–multiprobe scheme is less adapted since the intervals between probe pulses (few ns) are longer than the timescale of the physical phenomena studied. However, it is still interesting to perform two acquisitions after each pump pulse (pump–probe–probe scheme): a first acquisition is taken shortly after the pump pulse in order to study the excited sample ('pumped' signal), and a second one is taken at a longer pump–probe delay when the sample is completely relaxed ('unpumped' signal). The 'unpumped' signal can then be used as a reference signal, which makes it possible to normalize the photo-induced relative changes of the diffracted intensity on a nearly shot-to-shot basis, and helps remove the drifts which might occur due to either instabilities of the incoming X-ray beam or to sample degradation. A simple way to measure quasi-simultaneously both the photo-induced signal (excited sample) and the reference signal (relaxed sample) is to run the detector at twice the frequency of the pump pulses.

In a classical pump–probe measurement, the detector is operated in the so-called stroboscopic mode which allows accumulation of the signal from many individual gates in every pixel counter before reading out the detector. This mode allows operation of detectors with a rather low frame rate at high laser repetition rates. The pump–probe–probe scheme described in this work requires reading out a detector after every individual gate, therefore operating it at high frame rates. The total accumulated signal for each probe (gate) is obtained by summing the acquired images. In this mode, the maximum laser repetition rate is determined by the maximum frame rate of the detector.

For hard X-ray scattering experiments, pump–multiprobe schemes have been achieved using point detectors in the form of an avalanche photodiode (APD) coupled with a dedicated data acquisition system (Britz *et al.*, 2016; Lima *et al.*, 2011; March *et al.*, 2011). Pump–probe–probe schemes have been achieved since 2004 (Saes *et al.*, 2004) at several synchrotron beamlines using APDs, including the CRISTAL beamline at SOLEIL. On the other hand, instruments based on 2D detectors capable of running in the MHz range frame rate have also been developed at free-electron laser facilities such as the European XFEL (Allahgholi *et al.*, 2019). However, to the best of our knowledge, the multiprobe technique has never been implemented with just a single 2D detector at synchrotron light sources, nor at free-electron laser facilities before this work. In order to fill this demand, a full two-chip camera (256 × 256 pixels) based on hybrid pixel technology has been developed at SOLEIL along with a dedicated data acquisition system. The new detector is based on the fast photon-counting UFXC32k readout chip developed by the AGH University in Krakow (Grybos *et al.*, 2016). The maximum frame rate is 50 kHz for the chip and 20 kHz for the camera, which makes it possible to perform pump–probe–probe measurements at a high repetition rate. At CRISTAL, the excitation repetition rate is usually lower than 10 kHz. A key advantage of the UFXC32k chip over the MHz detectors developed for European XFEL is its relatively small pixel size (75 µm versus 200 µm or more), which will be an asset when studying the details of diffraction peak profiles.

In this work, we present the first experiments performed at CRISTAL with the two-chip UFXC32k camera, using both laser and X-ray beams. Section 2 summarizes all the intrinsic performances of the UFXC32k chip and describes the integration of the UFXC32k chips into a dedicated DAQ system developed at SOLEIL. In Section 3, we show that the mechanical design of the camera allows efficient shielding against laser-photon detection and laser-related electromagnetic perturbations. Section 4 presents the measurements of the variation of the diffraction signal related to the propagation of a laser-induced strain wave in InSb, using the pump–probe–probe scheme. The experimental data obtained show how the reference signal acquired with the second probe can be used to efficiently reduce fluctuations due to drifts of the experimental conditions.

2. The two-chip camera prototype

The fast single-photon-counting camera developed at SOLEIL consists of a hybrid pixel detector based on the UFXC32k readout chip (Grybos *et al.*, 2016). The UFXC32k circuits are bump bonded to silicon sensors. Single-chip prototypes were first fabricated and successfully tested at different beamlines in SOLEIL (Dawiec *et al.*, 2017; Koziol *et al.*, 2018; Bachiller-Perea *et al.*, 2019). After the validation of these first prototypes, a full two-chip camera was designed and developed (Dawiec *et al.*, 2019). This project involved the conception and realization of the three different parts of the camera: the detector (chips and detector carrier board), the data acquisition system (DAQ) with an embedded field-programmable gate array (FPGA) and the server with its specific software. The mechanical and cooling systems have also been developed within the frame of this project.

Table 1
Main features of the UFXC32k chip.

X-ray energy	From 5 to a few tens of keV (depending on the sensor material)
Pixel size (µm)	75 × 75
Number of pixels	128 × 256 = 32768
Detection surface (mm)	9.6 × 19.2
Discriminators	2 (low, high)
Counters	2 of 14 bits with programmable depth (1 × 28, 2 × 14, 2 × 8, 2 × 4, 2 × 2 bits)
Frame rate (kHz)	Up to 50
Linear count rate (photons s^{-1} mm^{-2})	∼4.6 × 10^8
10% error (photons s^{-1} $pixel^{-1}$)	∼2.6 × 10^6

2.1. Features of the UFXC32k readout chip

The UFXC32k chip was designed by the AGH University in Krakow (Grybos *et al.*, 2016). The main features of this readout chip are summarized in Table 1.

The description, characterization and validation of this single-photon-counting chip have already been described in previous works (Dawiec *et al.*, 2017; Koziol *et al.*, 2018). However, it is worth mentioning here the key features that make this readout chip suitable for pump–probe–probe experiments: (i) a frame rate up to 50 kHz which permits us to take more than one image after each pump pulse; (ii) a moderated pixel size of 75 µm × 75 µm; (iii) a linear count-rate for fluxes up to ∼4.6 × 10^8 photons s^{-1} mm^{-2}; (iv) the possibility of having a short exposure time (down to 80 ns); (v) two thresholds and two counters that allow for suppression of the background noise at low energies (low counter) and the spurious signals at high energies coming from the beam harmonics and from the pile-up at high photon fluxes (high counter).

The combination of all these properties makes the UFXC32k circuit a promising readout chip for time-resolved experiments using synchrotron radiation.

2.2. Architecture of the two-chip camera

Fig. 1 shows a sketch of the three main parts of the camera (detector, DAQ system and server) and the connections between them. The main features of the architecture are summarized below, but more details can be found in the work by Dawiec *et al.* (2019).

The detector consists of two UFXC32k chips separated by a one-pixel-sized gap (75 µm). The material that has been used for the sensor of this camera is 320 µm-thick silicon, which is suitable for detecting photons in the range 5–10 keV with an efficiency higher than 90% and in the range of 10–15 keV with efficiencies of 90–50%. The Si sensor has 256 × 256 pixels with larger pixels over the gap region (1.5 times the normal size), covering both UFXC32k chips and the 75 µm gap, and allowing for correction of the column of virtual pixels between the two readout chips (after correction the image has 256 × 257 pixels). Therefore, the effective surface of the detector is 1.92 cm × 1.93 cm.

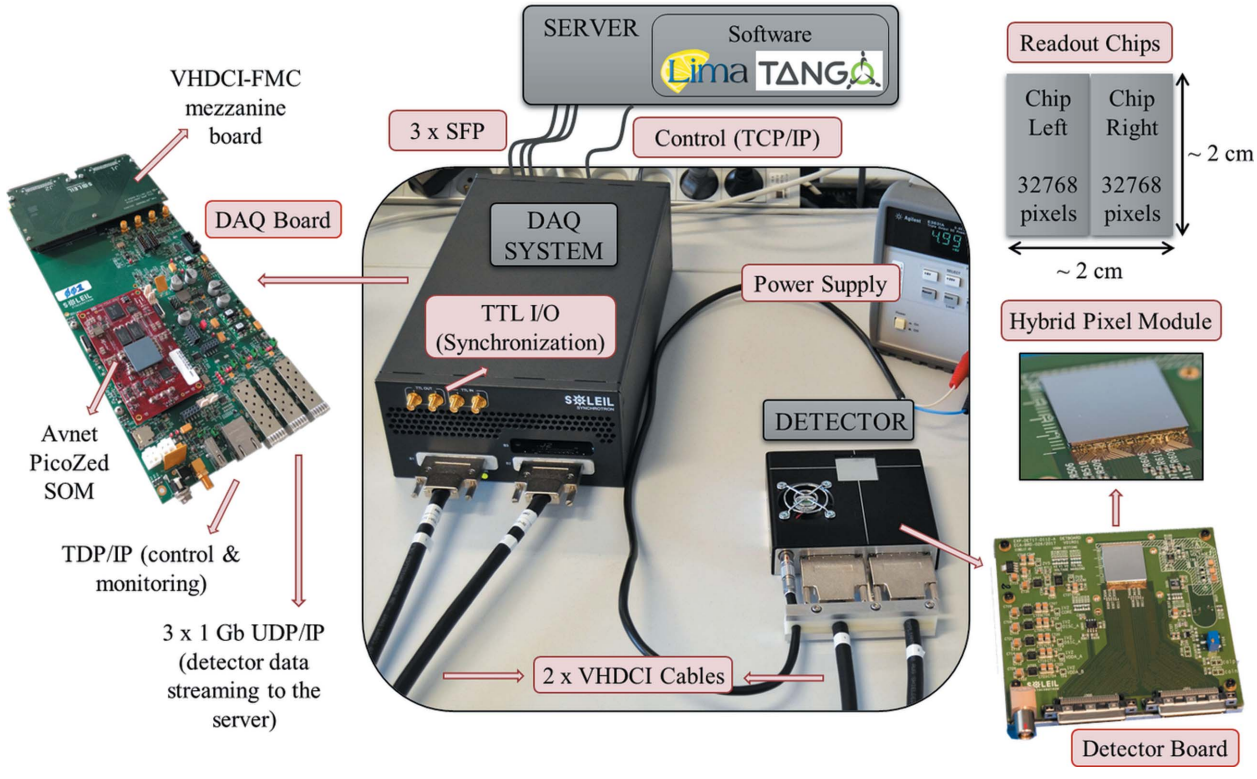

Figure 1
Main elements of the two-chip camera. Central picture: detector connected to the DAQ system by two VHDCI cables. On the right: detector board and hybrid pixel module. On the left: data acquisition board.

The mechanical design of the detector consists of an aluminium housing with the entrance window covered by an aluminized Mylar foil (polyethylene terephthalate with 20 nm of aluminium). The air fan opening in the housing has been partially covered with a 25 µm-thick aluminium foil.

The detector board is connected to the DAQ board by two VHDCI (very-high-density cable interconnect) cables, one per readout chip. The synchronization of the detector with external signals or devices is achieved via four TTL connectors (two for input and two for output). The data are transferred to the server using 1 Gb Ethernet UDP/IP Protocol over three SFP (small form-factor pluggable) ports. An Ethernet TCP/IP connection between the server and the DAQ board permits the control and monitoring of the detector.

Two functioning modes of the detector have been implemented in the firmware of the DAQ board FPGA: (i) a standard mode in which the detector is counting during the whole specified acquisition time, 14 bits are used for each counter; and (ii) a gated mode in which the detector only counts for a short period of time (80–120 ns) when the external trigger signal is detected. The short duration of the counting times permits extraction of the signal from a single X-ray bunch when SOLEIL is operated in a time-resolved mode (synchrotron light pulses are then separated by 147.5 ns). Only 2 bits per counter are used in the gated mode in order to shorten the readout time. This is the mode that is suitable for pump–probe(–probe) experiments. It allows us to acquire up to 65 536 images that are internally summed into two final images corresponding to the pumped and unpumped acquisitions. However, the current version of the software and server only allows us to acquire up to 20 000 images. This issue will be solved with the new version of the software API that is currently under development.

The characteristics of the synchrotron beam pulses make it impossible for a photon pixel detector to discriminate photons from a single electron bunch on the same pixel. Therefore, it is enough to read only the least significant bit from every pixel counter between individual gates. In the case of the UFXC32k readout chip, the minimum number of bits that can be read is two; as mentioned before, this readout mode is used in the gated acquisition mode. In order to make sure that the detector is operated within its linear count-rate region, the second threshold is set at a value higher than the beam energy to detect potential piled-up events.

Dedicated software libraries have been developed for this detector; they are compatible with the TANGO controls software which is used at SOLEIL.

3. Validation tests of the two-chip camera

In the first step the detector was extensively tested in the laboratory, where the characterization and corrections of the detector were performed. Then, in the second step the detector was tested at the CRISTAL beamline to validate the gated acquisition mode and the behavior of the detector in the laser environment.

3.1. Characterization and corrections applied to the camera

The measurements performed to characterize the detector and to prepare the configuration files were carried out using an X-ray generator at the Detector Laboratory in SOLEIL. The first results of the characterization (*e.g.*, offset spread, threshold dispersion, bad pixels, energy resolution) obtained with a temporary data acquisition system were published by Dawiec *et al.* (2019). Subsequently, we have performed additional measurements with the full camera including the new DAQ system in order to obtain the offset correction and the energy calibration of the chip.

The detector has two possible configurations of the gain settings: the low-gain configuration which is more suitable for energies above 8 keV, and the high-gain setting which is more suited for lower energies. All the characterizations and corrections have been performed for both gain settings.

The fluorescence of four different elements (5.9 keV from Mn, 8.0 keV from Cu, 9.9 keV from Ge, and 14.1 keV from Sr) was used for homogeneously illuminating the detector surface and for obtaining the configuration files with the offset correction for each pixel. These correction files are used to reduce the threshold dispersion of the pixels from 37% to 2.1%. After applying the offset correction, we performed threshold scans for the four previous energies; Fig. 2(*a*) shows, as an example, some of the measured scans (for the high-gain configuration). With the four pairs of threshold-energy values obtained from the inflection points of the averaged S-curves, we determined the energy calibration parameters for both readout chips, for each counter and for the two available gain configurations. Some of the results obtained for the high-gain configuration are shown in Fig. 2(*b*). The energy resolution was calculated by differentiating the threshold scan curves [Fig. 2(*c*)].

3.2. Tests at the CRISTAL beamline

Once the detector was configured and calibrated, it was tested at the CRISTAL beamline to (i) validate both functioning modes (standard and gated) with a temporary data acquisition system, and (ii) study the influence of laser-induced electromagnetic fields on the detector.

The experimental setup for this test is shown in Fig. 3. The diffraction ring of a Teflon (polytetrafluoroethylene – PTFE) sample was observed with the camera prototype. The energy of the X-ray beam was 7.07 keV, and the filling mode of the synchrotron was the eight-bunch mode: one bunch every 147.5 ns with a bunch duration (FWHM) of ∼90 ps. The X-ray beam was impinging with a grazing incidence angle on the PTFE target. The detector was placed at an angle of ∼20.5° with respect to the incident beam, which corresponds to the angle of the PTFE diffraction ring.

The laser system is a regenerative titanium:sapphire amplifier, providing 800 nm pulses with duration of 25 fs (FWHM) at a repetition rate of 1 kHz. The power of the laser was set to ∼1.3 W and the illumination was set up for two different angles of incidence: 10° and 90° with respect to the sample surface (the laser fluence being 2.3 mJ cm^{-2} pulse^{-1}

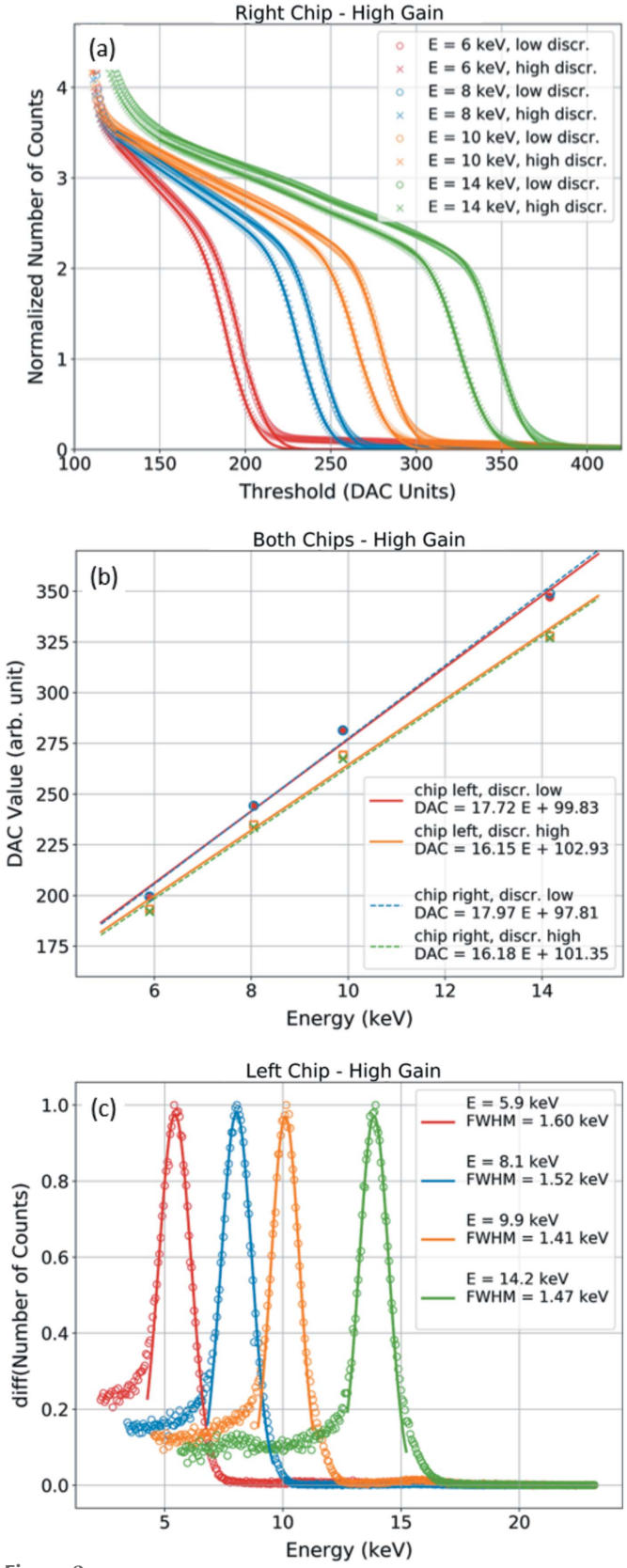

Figure 2
(*a*) Averaged threshold scans obtained during detector characterization in the laboratory with the high-gain configuration for the right chip. (*b*) Linear fits to obtain the energy calibration for the high-gain configuration for both chips (the two fits for the low/high discriminator overlap). (*c*) Energy resolution obtained from the threshold scans for the left chip.

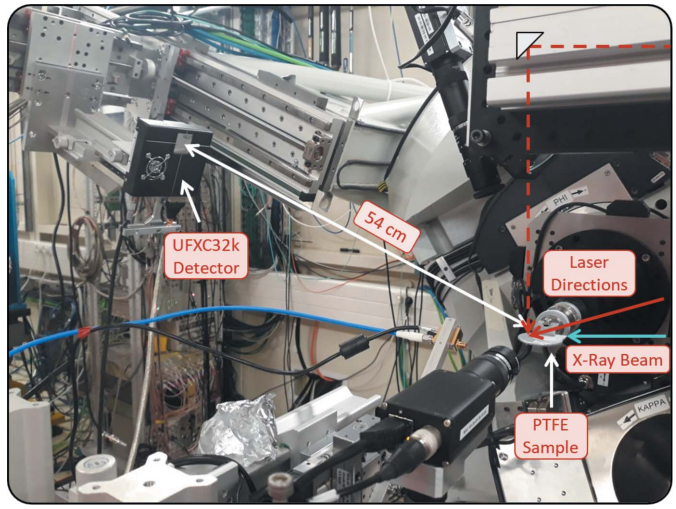

Figure 3
Experimental setup used at the CRISTAL beamline for the validation of the detector. Dashed red line: 90° laser incidence. Solid red line: 10° laser incidence. Blue line: X-ray beam direction.

and 13.5 mJ cm^{-2} pulse^{-1}, respectively). These two configurations reproduce the experimental conditions as close as possible to those used during normal user operation. In order to not damage the PTFE sample and deliberately increase the laser diffusion towards the detector, the laser beam impinged on a metallic surface (see Fig. 3).

Fig. 4 shows the images of the PTFE diffraction ring obtained by accumulating 20 images of 5 s with the standard acquisition mode. The energy threshold for both counters was set at 3.5 keV (half of the X-ray beam energy) to reduce the charge-sharing effect (Brönnimann *et al.*, 2000). The flat-field correction (Procz *et al.*, 2011) has been applied to these images in order to eliminate pixel-to-pixel variations due to sensor inhomogeneities and residual threshold dispersion. For this a series of 1000 images of 1 s acquisition time was taken with uniform detector illumination at 7.07 keV. The images shown in Fig. 4 are corrected by the so-obtained flat-field image. In addition, the noisy and dead pixels have been set to zero. Finally, the inter-chip gap has been corrected by adding a column of virtual pixels. Similar images were taken with the gated mode, which was also working properly. Therefore, both

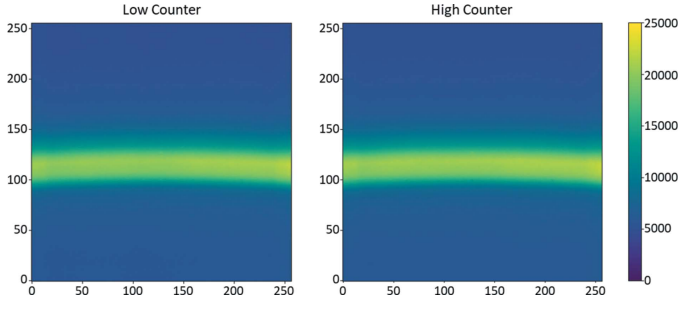

Figure 4
Images of the PTFE diffraction ring obtained with an acquisition time of 100 s for both low (left) and high (right) counters.

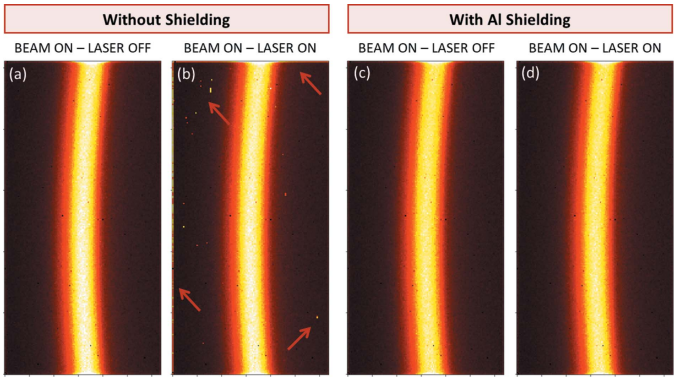

Figure 5
Images taken with one of the two chips of the detector and with the laser impinging on the metallic target with normal incidence. (*a*) and (*b*) Detector without shielding, with the laser off and on, respectively. (*c*) and (*d*) Detector with an Al shielding, with the laser off and on, respectively.

acquisition modes (standard and gated) were validated at the beamline.

Finally, images were acquired with and without the laser illumination in the two experimental configurations mentioned above (angle of incidence of the laser = 10°, 90°). When the angle of incidence of 10° was used, no influence of the laser radiation could be observed on the images. However, with the perpendicular incidence configuration, some pixels were revealed to be sensitive to laser illumination [Figs. 5(*a*) and 5(*b*), the arrows indicate some of the noisy pixels]. Note that, in this configuration, the footprint of the laser on the metallic target is ∼6 times smaller than when using 10° incidence. As a consequence, the laser intensity is ∼6 times larger, and the amplitude of the electric field is increased by a factor ∼2.4 since $|E|^2 \propto I$. Obviously, the 90° incidence configuration enhances the electromagnetic radiation which increases the electronic noise of the detector. However, this issue can be overcome by improving the shielding using a thin Al foil (<50 µm thick) [Figs. 5(*c*) and 5(*d*)].

These measurements proved that (i) the detector can be well integrated at the CRISTAL beamline, (ii) both acquisition modes (continuous and gated) are working properly and (iii) the spurious signals of the few laser-sensitive pixels can be suppressed by using a thin Al shielding.

4. Measurements of the photo-induced strain in InSb at the CRISTAL beamline

The second test carried out at the CRISTAL beamline (the first with the complete two-chip camera) aimed at testing the pump–probe–probe acquisition mode under real experimental conditions. To this end, the photo-induced acoustic response of an InSb crystal was measured by means of X-ray diffraction (XRD) [Fig. 6(*a*)].

When a solid sample is illuminated by a femtosecond laser pulse, the temperature of its surface increases suddenly. This results in a stressed layer that subsequently expands and launches a strain wave which propagates at the speed of sound

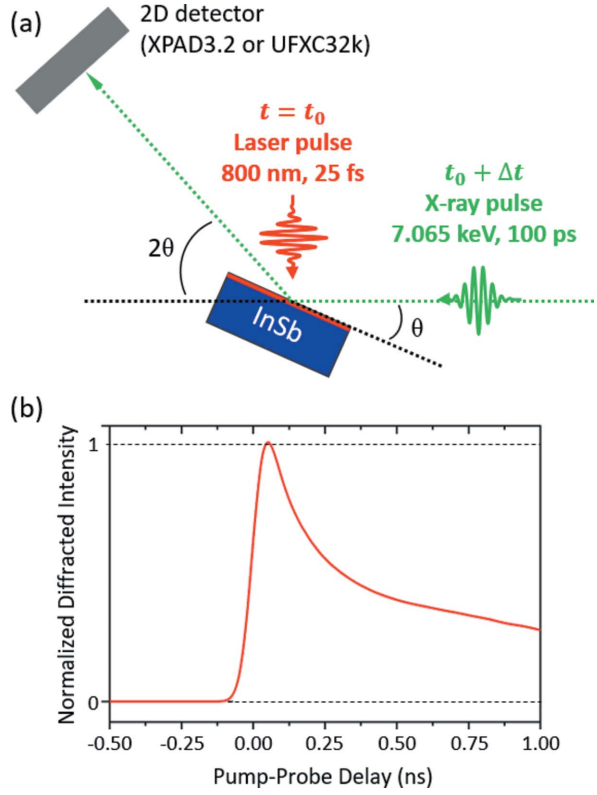

Figure 6
(*a*) Sketch of the incident pulses (laser and X-rays) impinging onto the InSb sample. (*b*) Simulation of the diffracted intensity observed at an angle slightly off the Bragg condition as a function of the pump–probe delay. The simulation was obtained using the *udkm1Dsim* toolbox (Schick *et al.*, 2014).

in depth of the sample. Observations of propagating strain waves in InSb have been extensively reported in the literature (Larsson *et al.*, 2002; Thomsen *et al.*, 1986), which allows for the design of a model experiment in this work. Fig. 6(*b*) presents a simulation of the time-dependent relative changes of the diffracted intensity for a crystal set slightly off the Bragg condition on the (111) peak, when it is traversed by a laser-induced strain wave. This constitutes the photo-induced signal that had to be experimentally measured.

4.1. Experimental setup

Fig. 7 shows the experimental setup used at the CRISTAL beamline for these measurements. The InSb (111) sample was placed on a six-circle diffractometer where it was excited (pumped) by 800 nm, 25 fs laser pulses at a repetition rate of 1 kHz. At this wavelength, the optical penetration depth in InSb is ∼90 nm. The laser beam impinged vertically on the sample surface, defining a footprint of 1 mm × 3.6 mm and an incident fluence of ∼5 mJ cm^{-2}. Synchrotron X-ray pulses of 7.105 keV energy and 90 ps duration were used to probe the InSb crystal. The (111) reflection was studied in a θ–2θ configuration [Fig. 6(*a*)]. At this energy, the Bragg condition is fulfilled for an incidence angle θ = 13.487° with respect to the (111) planes. The photo-induced signal was measured out of Bragg condition, by setting θ = 13.444°.

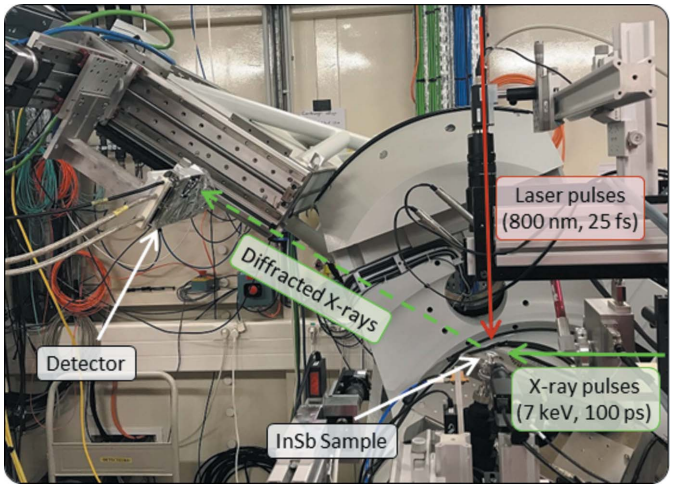

Figure 7
Experimental setup used at the CRISTAL beamline for the measurements. The green arrows indicate the directions of the incident and diffracted X-ray photons. In red, the trajectory of the laser beam that excites the sample.

The laser pulses were electronically phase-locked to a single electron bunch in the storage ring, allowing synchronization between the laser pulse and the X-ray probe with an accuracy of 5 ps. In order to acquire the XRD signal arising from the strained InSb as a function of time, the time delay between the X-ray pulses and the laser pulses ($\Delta t = t - t_0$) was progressively increased. For each time delay, the XRD signal was measured by the UFXC32k detector in the pump–probe–probe scheme: two images were taken after each laser pulse. Since the repetition rate of the laser was 1 kHz, the frequency of the UFXC32k camera was set at 2 kHz. The chronogram of the experiment is shown in Fig. 8. The first image is acquired at time Δt and measures the XRD intensity when the InSb sample is in an excited state (pumped signal); the second image is acquired at time Δt + 500 µs and measures the XRD intensity when the sample has returned to its relaxed state (unpumped signal). By varying the delay time Δt we can determine the variation of the XRD intensity as a function of time and obtain a curve similar to the one shown in Fig. 6(*b*).

Table 2
Main features of the UFXC32k and XPAD3.2 detectors.

	UFXC32k	XPAD3.2
Sensor	Si – 320 µm	Si – 500 µm
Maximal count rate (photons s^{-1} $pixel^{-1}$)	~2.6×10^6	~2×10^5
Maximal count rate (photons s^{-1} mm^{-2})	~4.6×10^8	~1.2×10^7
Pixel size (µm)	75 × 75	130 × 130
Number of pixels	256 × 256 = 65792	560 × 960 = 537600
Detection surface (cm)	1.92 × 1.93	7.5 × 15
Gate duration (ns)	80–120	≥80
Time-resolved possibilities	Pump–probe–probe	Pump–probe

In order to validate and evaluate the advantages of the new UFXC32k camera, it has been compared with the detector which is currently used at the beamline for this type of experiment: an XPAD3.2 detector (Pangaud *et al.*, 2007). A comparison of the main features of both UFXC32k and XPAD3.2 detectors is presented in Table 2, which shows that the XPAD3.2 detector has a larger detection surface that eases the Bragg-peak search. On the other hand, the UFXC32k detector has a linear count-rate for higher fluxes, smaller pixels and permits the implementation of pump–probe–probe experiments at a high repetition rate, which is not possible with XPAD3.2. In both measurements, the detectors were placed at the same distance from the sample (~50 cm). The detectors were synchronized to the same electron bunch as the laser and the length of their gate was chosen in such a way that only the X-ray photons coming from the synchronized bunch are measured.

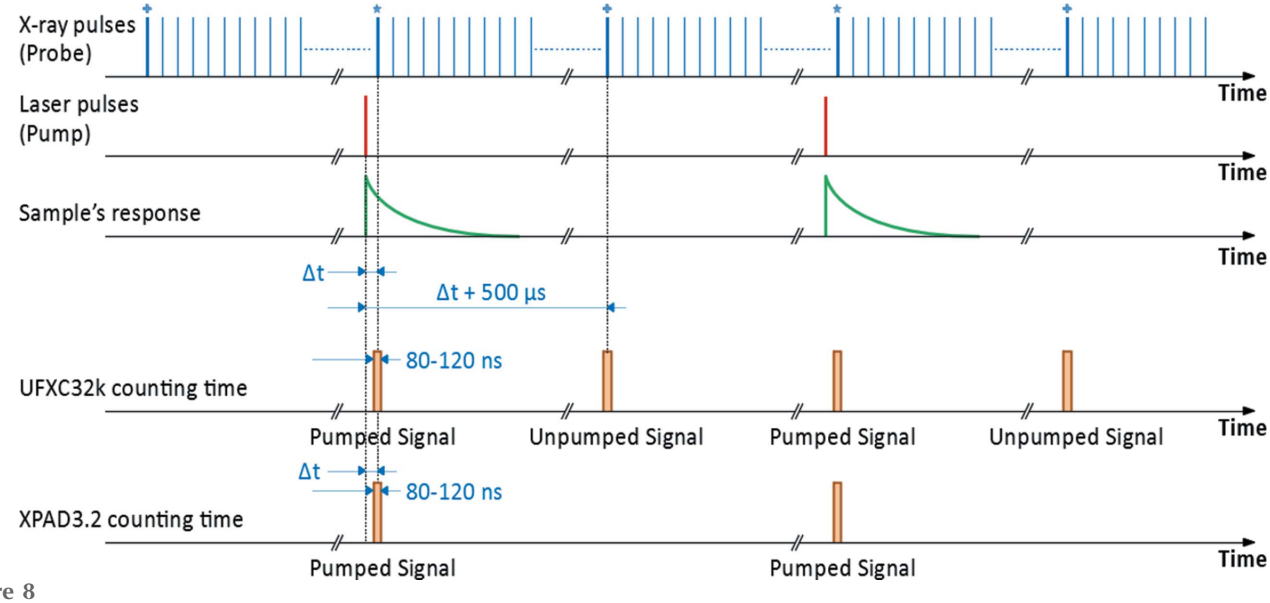

Figure 8
Chronogram of the time-resolved experiment held at the CRISTAL beamline, showing the arrival times of laser and X-ray pulses, as well as the electronic gates that define the counting periods of both UFXC32k and XPAD3.2 detectors.

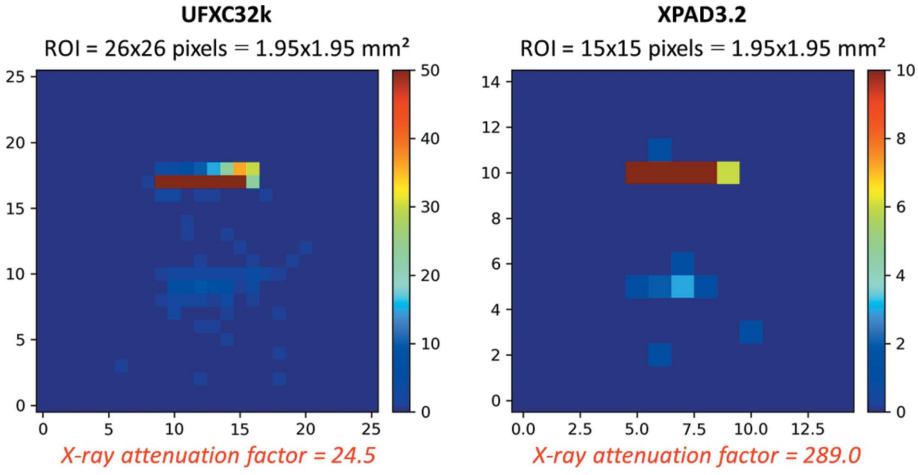

Figure 9
Images of the diffracted beam obtained by accumulating 1000 gates with the UFXC32k detector (left) and the XPAD3.2 detector (right). The regions of interest presented here were chosen so that the physical area of both images are the same (1.95 mm × 1.95 mm).

4.2. Results and discussion

Fig. 9 shows the images of the diffracted beam acquired by the UFXC32k and XPAD3.2 detectors at a fixed pump–probe delay of −0.5 ns (*i.e.*, before laser excitation) for an exposure time of 1 s (accumulation of 1000 gates). The diffracted flux from the sample was measured to be $\sim 2 \times 10^{10}$ photons s^{-1} mm^{-2}. Since the maximum flux for which the detectors have a linear behavior is $\sim 4.6 \times 10^{8}$ photons s^{-1} mm^{-2} for UFXC32k and $\sim 1.2 \times 10^{7}$ photons s^{-1} mm^{-2} for XPAD3.2, the X-ray beam had to be attenuated with different attenuation factors for each detector: 24.5 for UFXC32k and 289.0 for XPAD3.2. As a consequence, the number of counts in the UFXC32k image is higher that the number of counts in the XPAD3.2 image. The advantage of the smaller pixel size of the UFXC32k detector (which allows for a better spatial resolution) is observed in Fig. 9 with the diffraction pattern selected.

The low energy threshold of the UFXC32k detector was set at half of the beam energy (3.5 keV) for reducing the charge-sharing effect. The high energy threshold was set at 10.0 keV in order to measure only the photons from the third harmonic with the high counter. For the analysis, only images recorded with the low counter have been used, the high counter was used to verify that the contribution of higher energy photons (third-harmonic contribution) was negligible. The threshold of the XPAD3.2 detector was set at ∼5 keV.

4.2.1. Measurements in pump–probe–probe mode. The time-dependent photo-induced signal measured with the UFXC32k camera can be seen in Fig. 10. For each value of Δt, the diffracted intensity is obtained as a sum of the photon counts over 1000 X-ray pulses and over the region of interest (ROI) shown in Fig. 9. The red curves correspond to the images taken during the first probe pulse when the sample is excited (pumped). These curves exhibit a time-dependent behavior which matches that simulated in Fig. 6(*b*). The blue curves correspond to the second probe when the sample has relaxed (unpumped). In absence of experimental drift, these signals are expected to be independent of Δt. Figs. 10(*a*) and 10(*b*) correspond exactly to the same measurement repeated twice. However, while Fig. 10(*a*) shows a very steady unpumped signal, Fig. 10(*b*) shows unsteady signals due to (very likely) instabilities on the beamline optics. This example, representative of real measurement conditions, illustrates the importance of the pump–probe–probe acquisition mode for the data analysis. Indeed, the advantage of this method is that we can normalize the pumped signal to the unpumped one for each pump–probe cycle [equation (1)]. The result of normalizing both data sets from Fig. 10 is shown in Fig. 11. One can observe that both normalized

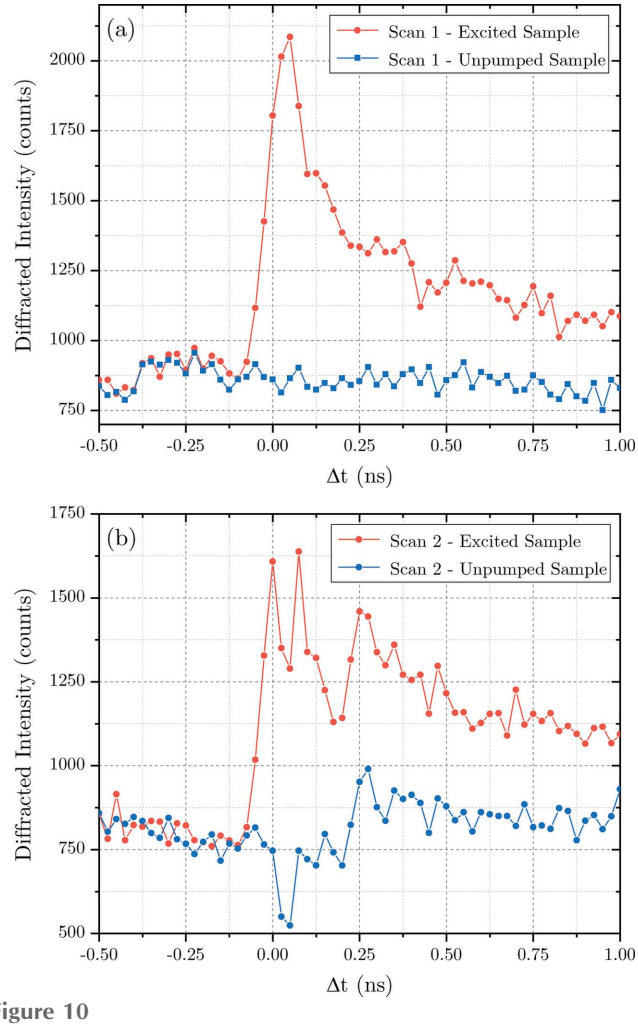

Figure 10
Two measurements of the photo-induced signal versus Δt obtained with the UFXC32k camera with identical experimental conditions. (*a*) During this measurement (Scan 1), the intensity of the incoming beam was steady. (*b*) In the second measurement (Scan 2), variations in the intensity of the incoming beam are observed.

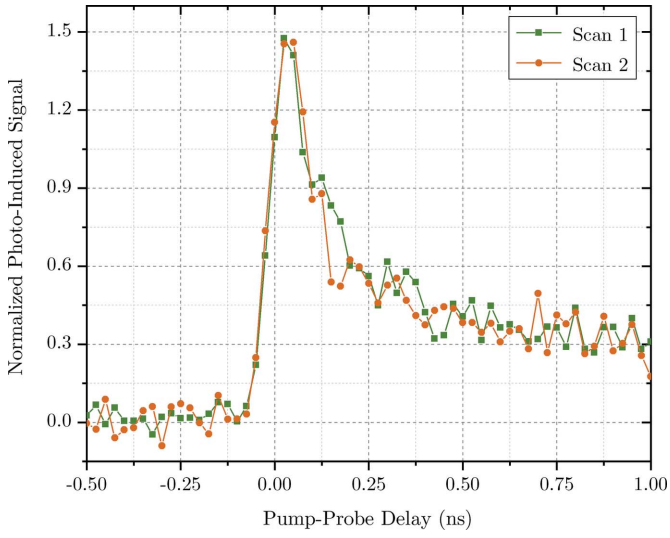

Figure 11
Photo-induced signal in InSb after normalization to the unpumped images. The variations on the beam intensity are corrected when applying the normalization and the same result is obtained for both measurements (Scans 1 and 2).

photo-induced signals are in good agreement, despite the fact that the data initially collected exhibited relative differences up to 46%. This shows that the impact of the drifts of the incoming X-ray beam can be limited by adopting a pump–probe–probe scheme, which we now propose for the first time with a 2D detector.

$$S_{\text{Normalized}}(\Delta t) = \frac{I_{\text{Excited}}(\Delta t) - I_{\text{Unpumped}}(\Delta t)}{I_{\text{Unpumped}}(\Delta t)}. \qquad (1)$$

4.2.2. Comparison to the present detector at the beamline. Finally, the same measurement was repeated with the XPAD3.2 detector. As previously mentioned, this detector can take only one probe image after each laser pulse. Therefore, the normalization of the pumped signal [equation (1)] can only be achieved by substituting $I_{\text{Unpumped}}(\Delta t)$ by the mean value of the diffraction intensity for $\Delta t < 0$ (*i.e.*, before the laser pulse arrives). As a result, it is not possible to correct the measured photo-induced signal on a shot-to-shot basis.

Fig. 12 shows the results obtained for both detectors (UFXC32k and XPAD3.2) by taking images of 2000 gates for each value of Δt. Both experimental signals (blue dots in the figure) are compared with a reference signal that was obtained by accumulating a greater number of statistics (220 000 gates, acquisition time of several hours) and by fitting these data to an *ad hoc* function (red curve in the plots). We can observe that the signal obtained with the UFXC32k detector fits much better than the XPAD3.2 signal to the reference.

To estimate the deviation of the experimental data with respect to the reference curve, we used parameter σ calculated using equation (2), where S_{exp} is the normalized intensity measured for each delay i and S_{ref} is the expected intensity calculated with the reference curve for that delay. For the data in Fig. 12(*a*) (UFXC32k, 2000 gates) we obtain σ = 0.364,

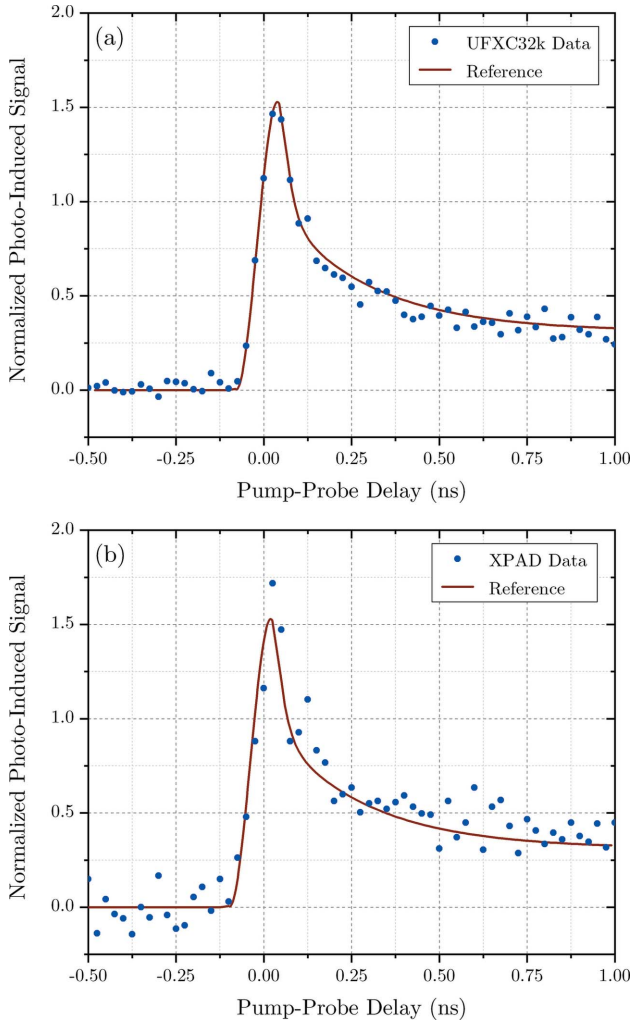

Figure 12
Experimental curves obtained with (*a*) UFXC32k and (*b*) XPAD3.2 superimposed to a reference curve.

whereas for the same number of gates with the XPAD3.2 detector we have σ = 0.919. Fig. 13 shows the value of σ for the XPAD3.2 detector as a function of the number of gates; one can observe that the value of σ = 0.364 is reached with ∼16000 gates. In fact, since the UFCX32k detector has a higher count-rate limit for its linearity region and requires less flux attenuation than the XPAD3.2 detector, we can obtain better statistics (by a factor of ∼8) with the UFXC32k camera, allowing for lower acquisition times,

$$\sigma = \left[\sum_i (S_{\text{exp},i} - S_{\text{ref},i})^2\right]^{1/2}. \qquad (2)$$

5. Conclusions and perspectives

A new two-chip single-photon-counting camera has been developed at the SOLEIL synchrotron to carry out multiple-probe diffraction experiments at a high repetition rate. This hybrid pixel detector was characterized and configured at the

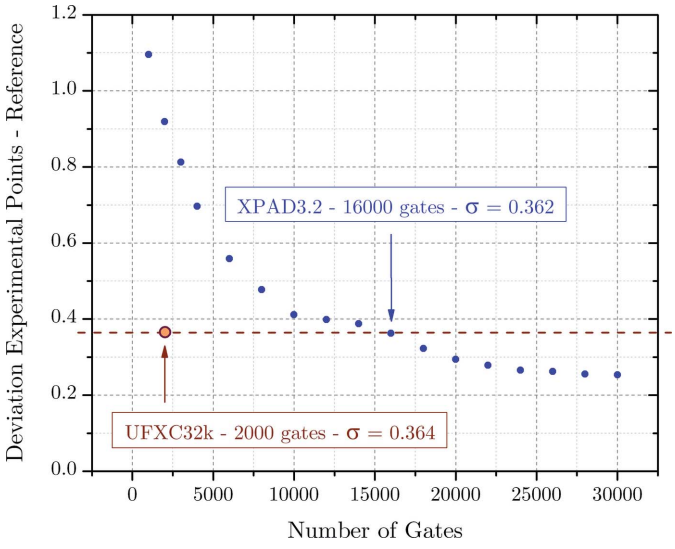

Figure 13
Deviation (σ) of the XPAD3.2 experimental data from the reference curve for different numbers of acquisition gates (violet dots). The value obtained for 2000 gates with the UFXC32k detector is given in brown.

Detector Laboratory and then integrated and validated at the CRISTAL beamline during a benchmark experiment. The compressive strain induced in InSb by laser pulses has been observed by measuring the corresponding time-dependent diffraction signal within a pump–probe–probe scheme. This experiment proved the extremely good performances of the new detector for time-resolved synchrotron-radiation-based experiments. The first advantage of the UFXC32k camera is the possibility of correcting intensity variations that are caused by experimental drifts by measuring a reference signal on a shot-to-shot basis. Other advantages with respect to the currently available detectors for pump–probe experiments are its readout speed and better spatial resolution.

Although this project originated from the interest of the CRISTAL beamline to improve time-resolved diffraction experiments, the use of the UFXC32k detector will be extended to other beamlines at SOLEIL due to the possibilities it offers for synchrotron techniques (*e.g.*, its high count-rate limit allows for better statistics with shorter acquisition times without damaging the detector). Other geometries of this type of detector dedicated to the specific needs of the beamlines are being developed. As an example, a 1 cm × 4 cm detector has been designed and is under fabrication for the ODE beamline (Baudelet *et al.*, 2011) to carry out energy-dispersive X-ray absorption spectroscopy. The development will expand to detectors with larger detection surfaces, for instance, we are currently working on the design of an eight-chip camera (4 cm × 4 cm). New detectors based on the same technology will be fabricated with thicker sensors (450 µm-thick Si) to increase the quantum efficiency at higher photon energies. In addition, new functioning acquisition modes of the UFXC32k will be implemented in the DAQ system and software, and will enlarge the possibilities of the experiments that can be carried out at the SOLEIL beamlines.

Acknowledgements

The authors would like to acknowledge P. Hollander for his help with the laser preparation and T. Marion for the information about the filling modes of the SOLEIL synchrotron.

Funding information

Authors from AGH-UST are supported by the National Science Center, Poland (contract No. UMO-2016/21/B/ST7/02228).

References

Allahgholi, A., Becker, J., Delfs, A., Dinapoli, R., Goettlicher, P., Greiffenberg, D., Henrich, B., Hirsemann, H., Kuhn, M., Klanner, R., Klyuev, A., Krueger, H., Lange, S., Laurus, T., Marras, A., Mezza, D., Mozzanica, A., Niemann, M., Poehlsen, J., Schwandt, J., Sheviakov, I., Shi, X., Smoljanin, S., Steffen, L., Sztuk-Dambietz, J., Trunk, U., Xia, Q., Zeribi, M., Zhang, J., Zimmer, M., Schmitt, B. & Graafsma, H. (2019). *J. Synchrotron Rad.* **26**, 74–82.

Bachiller-Perea, D., Baudelet, F., Coquet, J., Kong, Q., Orsini, F. & Dawiec, A. (2019). *Nucl. Instrum. Methods Phys. Res. A*, **936**, 547–548.

Baudelet, F., Kong, Q., Nataf, L., Cafun, J. D., Congeduti, A., Monza, A., Chagnot, S. & Itié, J. P. (2011). *High. Press. Res.* **31**, 136–139.

Britz, A., Assefa, T. A., Galler, A., Gawelda, W., Diez, M., Zalden, P., Khakhulin, D., Fernandes, B., Gessler, P., Sotoudi Namin, H., Beckmann, A., Harder, M., Yavaş, H. & Bressler, C. (2016). *J. Synchrotron Rad.* **23**, 1409–1423.

Brönnimann, C., Florin, S., Lindner, M., Schmitt, B. & Schulze-Briese, C. (2000). *J. Synchrotron Rad.* **7**, 301–306.

Dawiec, A., Abiven, Y.-M., Bachiller-Perea, D., Bisou, J., Kanouté, B., Menneglier, C., Orsini, F., Sergent, Y. & Thibaux, G. (2019). *AIP Conf. Proc.* **2054**, 060067.

Dawiec, A., Maj, P., Ciavardini, A., Gryboś, P., Laulhé, C., Menneglier, C. & Szczygiel, R. (2017). *J. Instrum.* **12**, C03057.

Grybos, P., Kmon, P., Maj, P. & Szczygiel, R. (2016). *IEEE Trans. Nucl. Sci.* **63**, 1155–1161.

Koziol, A., Bordessoule, M., Ciavardini, A., Dawiec, A., Da Silva, P., Desjardins, K., Grybos, P., Kanoute, B., Laulhe, C., Maj, P., Menneglier, C., Mercere, P., Orsini, F. & Szczygiel, R. (2018). *J. Synchrotron Rad.* **25**, 413–418.

Larsson, J., Allen, A., Bucksbaum, P. H., Falcone, R. W., Lindenberg, A., Naylor, G., Missalla, T., Reis, D. A., Scheidt, K., Sjögren, A., Sondhauss, P., Wulff, M. & Wark, J. S. (2002). *Appl. Phys. Mater. Sci. Process.* **75**, 467–478.

Laulhé, C., Cammarata, M., Servol, M., Miller, R. J. D., Hada, M. & Ravy, S. (2013). *Eur. Phys. J. Spec. Top.* **222**, 1277–1285.

Laulhé, C., Ravy, S., Fertey, P., Elkaim, E., Legrand, F., Féret, P., Hollander, Ph., Hustache, S., Bordessoule, M., Ricaud, J.-P., Collet, E., Lorenc, M., Buron-Le Cointe, M., Cailleau, H., Tissot, A. & Boillot, M.-L. (2012). *Acta Phys. Pol. A*, **121**, 332–335.

Lima, F. A., Milne, C. J., Amarasinghe, D. C. V., Rittmann-Frank, M. H., van der Veen, R. M., Reinhard, M., Pham, V.-T., Karlsson, S., Johnson, S. L., Grolimund, D., Borca, C., Huthwelker, T., Janousch, M., van Mourik, F., Abela, R. & Chergui, M. (2011). *Rev. Sci. Instrum.* **82**, 063111.

March, A. M., Stickrath, A., Doumy, G., Kanter, E. P., Krässig, B., Southworth, S. H., Attenkofer, K., Kurtz, C. A., Chen, L. X. & Young, L. (2011). *Rev. Sci. Instrum.* **82**, 073110.

Moonshiram, D., Garrido-Barros, P., Gimbert-Suriñach, C., Picón, A., Liu, C., Zhang, X., Karnahl, M. & Llobet, A. (2018). *Chem. Eur. J.* **24**, 6464–6472.

Pangaud, P., Basolo, S., Chantepie, B., Clemens, J. C., Delpierre, P., Dinkespiler, B., Menouni, M., Bonissent, A., Debarbieux, F. & Morel, C. (2007). *IEEE Nucl. Sci. Symp. Conf. Rec.* **1**, 14–18.

Procz, S., Pichotka, M., Lubke, J., Hamann, E., Ballabriga, R., Blaj, G., Campbell, M., Fauler, A., Mix, M., Zwerger, A. & Fiederle, M. (2011). *IEEE Trans. Nucl. Sci.* **58**, 3182–3189.
Saes, M., van Mourik, F., Gawelda, W., Kaiser, M., Chergui, M., Bressler, C., Grolimund, D., Abela, R., Glover, T. E., Heimann, P. A., Schoenlein, R. W., Johnson, S. L., Lindenberg, A. M. & Falcone, R. W. (2004). *Rev. Sci. Instrum.* **75**, 24–30.
Schick, D., Bojahr, A., Herzog, M., Shayduk, R., von Korff Schmising, C. & Bargheer, M. (2014). *Comput. Phys. Commun.* **185**, 651–660.
Silly, M. G., Ferté, T., Tordeux, M. A., Pierucci, D., Beaulieu, N., Chauvet, C., Pressacco, F., Sirotti, F., Popescu, H., Lopez-Flores, V., Tortarolo, M., Sacchi, M., Jaouen, N., Hollander, P., Ricaud, J. P., Bergeard, N., Boeglin, C., Tudu, B., Delaunay, R., Luning, J., Malinowski, G., Hehn, M., Baumier, C., Fortuna, F., Krizmancic, D., Stebel, L., Sergo, R. & Cautero, G. (2017). *J. Synchrotron Rad.* **24**, 886–897.
Thomsen, C., Grahn, H. T., Maris, H. J. & Tauc, J. (1986). *Phys. Rev. B*, **34**, 4129–4138.
Tordeux, M. A., Barros, J., Bence, A., Brunelle, P., Hubert, N., Pollina, J.-P. & Evain, C. (2012). *Proceedings of the 2012 International Particle Accelerator Conference (IPAC12)*, 20–25 May 2012, New Orleans, USA, pp. 1608–1610.